ORIGINAL ARTICLE

lajss.org
Latin American Journal of Solids and Structures

www.lajss.org

Study on the penetration of elliptical cross-section projectiles into concrete targets: theory and experiment

Junwei Liu[a], Xianfeng Zhang[a*], Haiyang Wei[a], Chuang Liu[a]

[a] School of Mechanical Engineering, Nanjing University of Science and Technology, Nanjing 210094, China. E-mails: liujunwei@njust.edu.cn, lynx@njust.edu.cn, why19960218@njust.edu.cn, chuang.liu@njust.edu.cn

* Corresponding author

https://doi.org/10.1590/1679-78256939

Abstract

To better understand the penetration mechanism of the elliptical cross-section projectile (ECSP) into semi-infinite concrete target, penetration experiments using three types of ECSPs with different shape ratios (1, 1.25 and 1.61) and with striking velocities ranged from 550 m/s to 1050 m/s were conducted. Penetration depths, penetration trajectory and mass erosion rates of the projectile were obtained after the experiments. The experiment results show that the penetration performance and ballistic stability of the ECSP are equivalent to those of the circular cross-section projectile (CCSP). Based on the theory of complex variable function and conformal transformation, a semi-analytical model which can calculate the cavity boundary stress distribution of elliptical section cavity controlled by the displacement boundary condition was established and the model was validated by comparing the model degenerate solution with Kirsch problem results. Theoretical calculation results show that the radial stress of elliptical section cavity increases progressively from the minor axis to the major axis. In addition, a formula combining with the semi-analytical theoretical model and the local interaction theory was developed. The predicted penetration depths were compared with 30 groups of experiment data with different projectile parameters and striking velocities and coincide quite well with the corresponding experimental data. Finally, the influence of shape ratio and caliber-radius-head (CRH) on the penetration performance of projectile and the application prospect of ECSPs on hypersonic weapon platform were studied.

Keywords

Elliptical cross-section projectile, Resistance characteristics, Conformal transformation

Graphical abstract

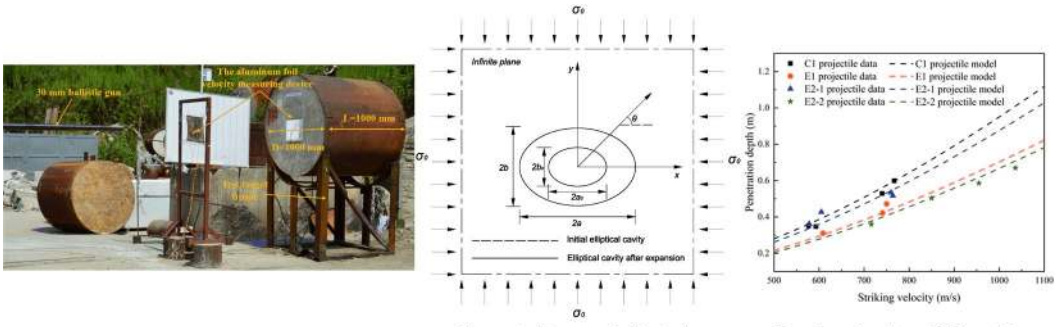

Layout of the experiment

Schematic diagram of elliptical cavity expansionment

Experiment and predictions data

Received: January 05, 2022. In Revised Form: Mach 13, 2022. Accepted: March 21, 2022. Available online: March 25, 2022
https://doi.org/10.1590/1679-78256939

Latin American Journal of Solids and Structures. ISSN 1679-7825. Copyright © 2022. This is an Open Access article distributed under the terms of the Creative Commons Attribution License, which permits unrestricted use, distribution, and reproduction in any medium, provided the original work is properly cited.

1 Introduction

The penetration performance of Earth-penetrating weapons on rock or soil media has been a research hotspot for many years. When the inherent parameters of the projectile such as striking velocities, material and mass remain unchanged, changing the projectile shape becomes a significant way to improve penetration performance of the projectile. Compared with the circular cross-section projectile (CCSP), the non-circular cross-section projectile has the advantages of excellent platform adaptability, high bending strength and improving the space utilization rate of the internal cavity of the platform [1-3]. Therefore, it is crucial to study the penetration performance, resistance characteristic and penetration mechanism of the non-circular cross-section projectiles, especially the elliptical cross-section projectile (ECSP), into rock or soil media.

For CCSPs, there are a lot of experience and engineering models that have been widely used in penetration problems [4-8], and can be well predict the penetration depth of projectiles, such as soil-disc model [4, 5] and cavity expansion model [6-8]. However, few studies are conducted to clarify the penetration mechanism of ECSPs. The research work of Ben-Dor et al. and Yakunina et al. [9-12] pointed out that when the projectile structure was formed by the surface of a circular cone and its tangential plane combination, the projectile has the smallest penetration resistance and the highest penetration efficiency. In 1978, Dhaliwal and Singh [13] gave the derivation process of the penetration force for the rigid projectile with arbitrary cross-section shape to punch into an elastic object, and proposed a simple closed-form expression of the penetration force required for projectiles with six types of cross-section shapes. Furthermore, HYUNG [14] proposed the cavity expansion problem with arbitrary cross section based on the least square method and concluded that the non-circular cross-section projectile structure can effectively reduce the penetration resistance of the target. However, due to the cavity boundary discretization method, this method cannot deal with continuous variable load problems and the accuracy of the calculation results is low. Bless [2] carried out high-speed penetration tests of rectangular cross-section rod and circular cross-section rod, compared and analyzed their penetration efficiency, and concluded that the penetration performance of asymmetric cross-section projectile was better below the critical velocity. In Petry and ACE (Army Corps of Engineers) [15, 16] empirical formulas, the residual velocity of non-circular projectiles is calculated using circular projectiles with the same cross-section area as non-circular projectiles. Wang et al. [17] carried out the penetration experiment of ECSPs and CCSPs, compared and analyzed the penetration performance of the two projectiles, and proposed an analysis model to calculate the penetration depth of the projectile based on the cavity expansion model. Nevertheless, the solution of the projectile penetration is simplified and the resistance model was still the traditional circular cavity expansion model, the model cannot reasonably explain the mechanism of the ECSP penetrating into concrete target.

Wu et al. and Liu et al. [18-20] carried out a series of penetration experiments of ECSPs penetrating into semi-infinite concrete target in the striking velocity range of 700 m/s to 1000 m/s and analyzed the penetration performance of the ECSP and the damage characteristics of the target. They studied the radial stress distribution along the circumferential direction at the cross-section of projectile nose through numerical simulation, introduced the shape factor of the ECSP to modify the cavity expansion theory, analyzed the variation law of the resistance of the projectile nose, and established the model of the normal penetration depth of the ECSP. However, the shape factor of the ECSP is obtained by fitting the numerical simulation results and its rationality require further verified. And it is unable to make a reasonable explanation for the causes of the circumferential stress distribution difference of the ECSP. Dai et al. [21] studied the penetration characteristics of the ECSP and analyzed the influence of CRH,axial stress, and resistance on penetration performance of the ECSP. Although the penetration mechanism of the ECSP was discussed in many aspects, the resistance expression in the theoretical model was still based on the dynamic cavity expansion theory, and the applicability of the resistance expression on ECSPs remains to be studied.

Practically, the penetration depth of the ECSP can be solved by converting the cross-sectional area of the ECSP into the area of an equivalent circle for engineering applications [15, 16]. However, due to the asymmetry of the ECSP, the radial stress distribution of the projectile nose and the response characteristics of the target are quite different from those of the CCSP [18-20]. The radial stress distribution characteristics of the ECSP nose are contributed to the structural optimization design of the projectile, the stability analysis of the charge and the oblique penetration trajectory of ECSPs. And the response characteristics of the target are crucial for understanding the asymmetric failure mode of the target. Unfortunately, the equivalent method focuses on macroscopic physical quantities such as penetration depth, and lacks discussion and research on the above problems.

As mentioned above, a wealth of research works on the penetration characteristics have been carried out, which promotes the study of the penetration mechanism of the ECSP. Nevertheless, there are still some limitations and more attention should be paid to the following aspects: (1) Experiments of ECSP penetration into semi-infinite concrete targets were conducted to have a better understanding of the penetration characteristics. (2) A semi-analytical model based on

the theory of complex variable function and conformal transformation [22, 23] was developed, which can calculate the stress distribution characteristics of elliptical section cavity. (3) A formula for predicting penetration depth was developed by taking the striking velocity, shape ratio and CRH of projectile into account combining with the semi-analytical model and the force characteristics on the projectile nose. And the formula was evaluated by the corresponding experimental data. (4) The influences of shape ratio and CRH on the penetration performance of projectile and the application prospect of ECSP on hypersonic weapon platform were analyzed and discussed.

2 Experimental study on the ECSP penetrating concrete

In order to study the penetration performance of ECSPs on concrete targets, a series of penetration experiments were conducted using four kinds of projectiles with shape ratios of 1, 1.25 and 1.56 (C1, E1, E2-1, E2-2). The experiments of four projectiles penetrating semi-infinite concrete target with striking velocities ranged from 550 m/s to 1050 m/s were carried out. After the experiment, the ballistic trajectory was obtained by splitting the concrete target and all the projectiles used in the penetration experiment were recovered.

2.1 Experimental program

The main parameters of the four projectiles are shown in Table 1. Notably, as can be seen from Ref. [21], the value of CRH of an ECSP varies with the azimuth. Namely, it increases progressively from the minor axis to the major axis along the circumference. Therefore, the values of CRH for each projectile at the major axis and the minor axis are noted in Table 1. In the following discussions, the value of CRH of the ECSP represents the CRH at the minor axis, that is, the maximum position on the projectile, and the value of CRH in the other directions can be calculated according to the size parameters of the projectile.

The diameter of C1 projectile is 24 mm and a caliber-radius-head (CRH) of 6.1. The semi-major and semi-minor of E2-1 and E2-2 projectiles are 15 mm and 9.6 mm. Particularly, the C1 projectile and the E2-1 projectile maintain the same cross-section area and mass, and the difference between them is that the shape ratio of cross-section is different, which is used to analyze the influence of the shape ratio of cross-section on the penetration performance.

The main difference between the two elliptical cross-section projectiles is that the mass of the E2-2 projectile is lower than that of the E2-1 projectile, which is realized by adjusting the depth and diameter of the inner hollows in their shanks, therefore the E2-2 projectile can have higher striking velocity in the experiments. The semi-major axis of the E1 projectile is 15 mm, and the semi-minor axis is 12 mm, which is used to study the influence of different shape ratios on the penetration performance. Four kinds of projectile head length are 58.1mm and the total length of the projectile are 144 mm, as shown in Fig. 1.

The experiment projectile is composed of projectile body and bottom-bolt. The projectile body material is 30CrMnSiNi2A, the density is 7.85 g/cm3, and the hardness is 42~45 HRC after quenching. The aluminum alloy is selected as the bottom-bolt material, which makes the projectile closely cooperate with the gun tube in the launch process to achieve excellent air closure effect and ensure the stability of the projectile launch.

The target used in the experiment is a concrete target of φ1000 × 1000 mm, and the average compressive strength is 40 MPa. The target is placed on the experiment target frame to ensure that the center height of the target is at the same height as that of the ballistic gun. The striking velocity was verified by the aluminum foil velocity measuring device and a high-speed photography. At the same time, the high-speed photography can observe the initial conditions of projectile entering the target. The experiment layout is shown in Fig. 2. In order to confirm the mechanical properties of concrete target, three cube samples with standard side length of 150 mm were poured and experimented. The compressive strength of the samples meets the design requirements.



(a) C1、E1 and E2-1 projectiles



(b) E2-2 projectile

Figure 1. Projectiles used in the experiment.

Table 1. Main parameters of CCSPs and ECSPs.

Name	Cross-section	2a(D) (mm)	2b(D) (mm)	Shape ratio	Cross-section area (mm2)	Mass (g)	Length (mm)	CRH
C1	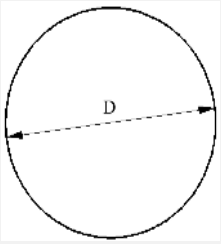	24	24	1	576	450	144	6.1/6.1
E1	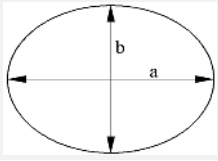	30	24	1.25	720	430	144	6.1/4.0
E2-1	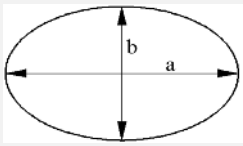	30	19.2	1.56	576	450	144	9.4/4.0
E2-2	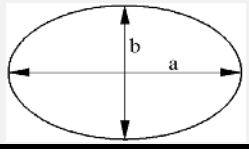	30	19.2	1.56	576	340	144	9.4/4.0

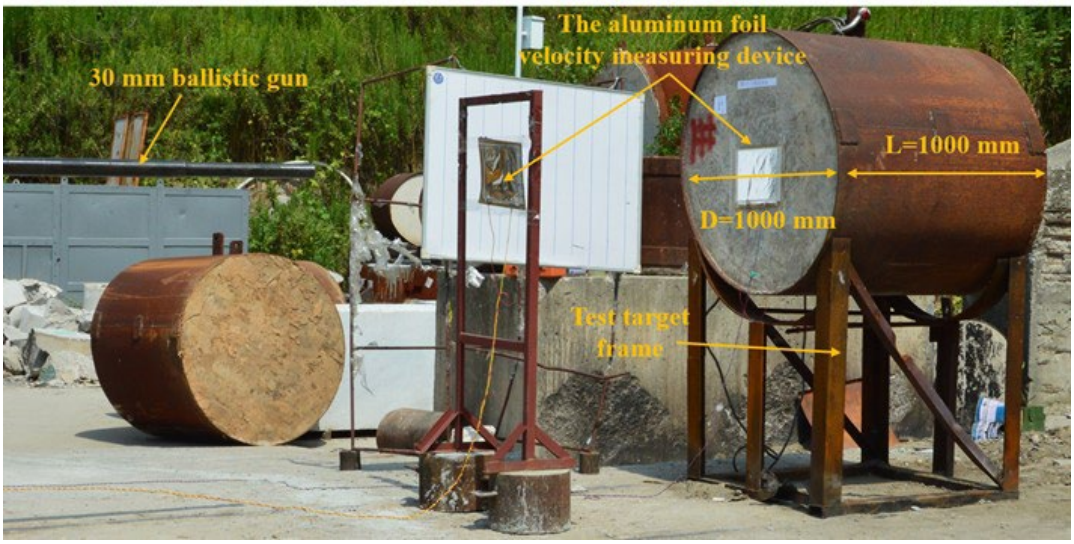

Figure 2. Layout of the experiment.

2.2 Experiment results and analyses

A total of 16 projectiles were launched in the experiment with striking velocities ranged from 550 m/s to 1050 m/s. The E1 projectile in experiment 6 bounced due to the large incident angle, so a total of 15 effective data were obtained. As shown in Table 2, the projectile striking velocity, penetration depth and mass loss ratio are counted after the experiment. The flying posture and trajectory of the E1 projectile in Test NO.7 are shown in Fig. 3 and Fig. 4, which indicates that the penetration condition can be regarded as normal penetration.

From the damage picture of the target (Fig. 5), it can be seen that the penetration process of ECSPs on concrete targets is similar to that of ordinary CCSPs, which is also composed of a crater stage and a tunnel stage. In addition, under the penetration of the ECSP, the tunnel shapes of ECSPs were similar to elliptical rather than round, which is significantly different from the CCSP. This phenomenon shows that during the penetration process of ECSPs, the materials around the elliptical cross-section cavity have different expansion velocities, which is different from the materials around the circular cross-section cavity. Therefore, the radial stress of the ECSP must be asymmetric.

Table 2. Measurements after the penetration experiment.

Test NO.	Type	Velocity (m/s)	Depth (m)	Mass (g)	Mass loss ratio (%)
1	C1	740	0.529	455	3.2
2	C1	767	0.599	453	2.8
3	C1	593	0.347	452	2.2
4	C1	577	0.351	453	2.3
5	E1	609	0.311	432	2.5
6	E1	/	/	/	/
7	E1	741	0.422	431	3.4
8	E1	750	0.472	431	3.3
9	E2-1	764	0.517	449	3.4
10	E2-1	760	0.534	449	2.7
11	E2-1	605	0.427	452	2.2
12	E2-1	578	0.362	453	1.9
13	E2-2	850	0.504	341	3.46
14	E2-2	1036	0.670	341	4.91
15	E2-2	716	0.360	339	4
16	E2-2	955	0.586	339	4.37



Figure 3. Attitude of E1 projectile in Test NO.7.

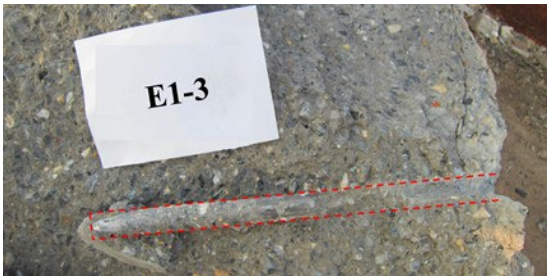

Figure 4. The E1 projectile trajectory in Test NO.7.

Fig. 6 is the penetration depth data of 15 projectiles under different striking velocities. Notably, the C1 projectile and E2-1 projectile have the same mass and cross-section area. It can be seen from the figure that the penetration depth of the C1 projectile is larger when the penetration velocity is about 750 m/s, and the average penetration depth is 7.3% higher than that of the E2-1 projectile. When the penetration velocity is about 600 m/s, the penetration depth of the E2-1 projectile is larger, and the average value is 13% higher than that of the C1 projectile. This shows that the ECSPs also have excellent penetration ability at high-speed striking velocity.

Compared with E1 projectiles, the values of CRH of E2-1 projectiles are larger, so the penetration ability of E2-1 projectile is significantly better than that of E1 projectile, which is consistent with the theory of Chen et al. [24, 25].

The penetration depth of E2-2 projectiles are generally low than others, because the total mass of E2-2 projectile is 90 g lighter than that of other projectiles. The penetration depth data of E2-2 can be used to verify the subsequent theoretical calculation model in a wide range of striking velocity. These experimental results provide a strong experimental data support for the structural optimization of the projectile. Because the penetration performance of the ECSP is similar to that of the CCSP, it means that the ECSP can be a choice to improve the space utilization of the hypersonic weapon platform. Fig. 7 is a typical recovered projectile after experiment and the relationship between the mass loss rate of the recovered projectile and the striking velocity. It can be seen from the figure that the noses and shanks remained intact and with the increase of the striking velocity, the mass loss rate increases, and the mass erosion rates of all projectiles is within 5%. Therefore, it can be considered that the projectile is in a rigid body penetration within striking velocities ranged from 550 m/s to 1050 m/s.



(a) Cater and tunnel for CCSP (b) Cater and tunnel for ECSP

Figure 5. Damage of concrete targets.

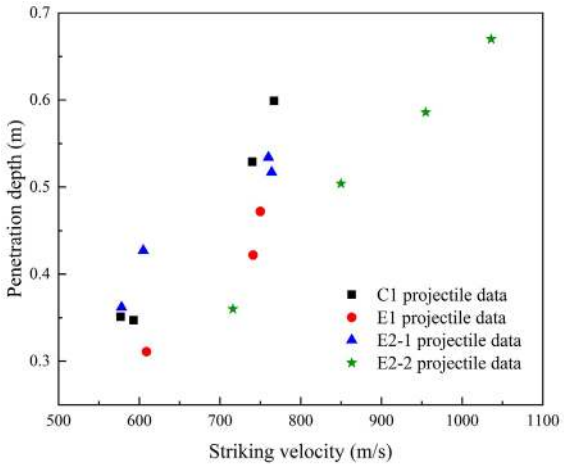

Figure 6. Penetration depth vs Striking velocity

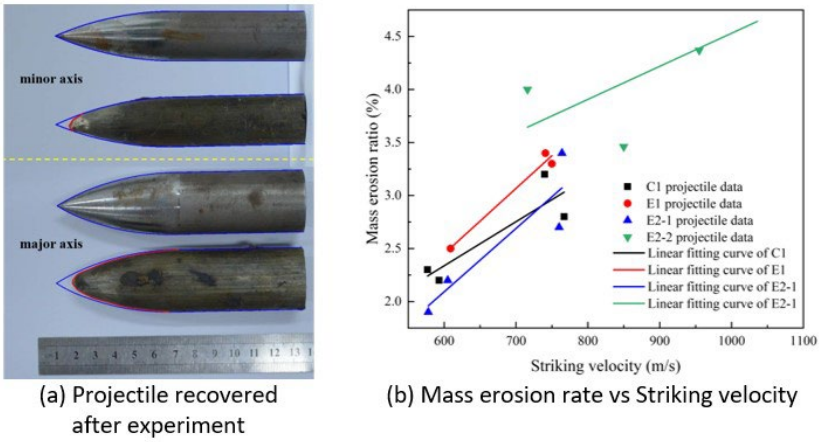

(a) Projectile recovered after experiment

(b) Mass erosion rate vs Striking velocity

Figure 7. Recovered projectile and mass erosion ratio.

3 Semi-analytical model of elliptical cavity expansion

3.1 Static elliptical cavity expansion model

3.1.1 Basic assumptions of the model

Considering a semi-infinite plane with an elliptical cavity (Fig. 8), the boundary of the elliptical cavity is controlled by displacement boundary conditions, and the stress state of the plane at infinity is known. Where a_0、b_0、a and b are structural parameters of the initial elliptical cavity and the elliptical cavity after expansion, respectively. σ_0 is the principal stress at infinity and θ is the polar angle in the Cylindrical coordinate system. The basic assumptions of the theoretical model are as follows:

(1) The material area can be approximated as an infinite single link and the deformation of the material is limited to a plane and satisfies the plane strain assumption;

(2) The plastic zone stress of the material satisfies the Von-Mises yield criterion.

(3) The shape ratio of elliptical cavity (a/b) remains constant during expansion.

(4) The plastic stress field of the cavity is statically determined, and no elastic unloading of the material [26-28].

3.1.2 Determination of the displacement boundary condition c assumptions of the model

The conformal mapping method developed by Muskhelishvili [23] is used to solve the second kind boundary-value problem of elasticity.

As shown in Fig. 9, the conformal mapping technique can transform the complex cavity boundary shape in the physical plane (*z* plane) into the unit circle in the phase plane (ζ plane) and simplify the solving process of complex cavity

boundary shape problem. r and θ are polar radius and polar angle in the physical plane, ρ and ϑ are polar radius and polar angle in the phase plane. The mapping transformation is

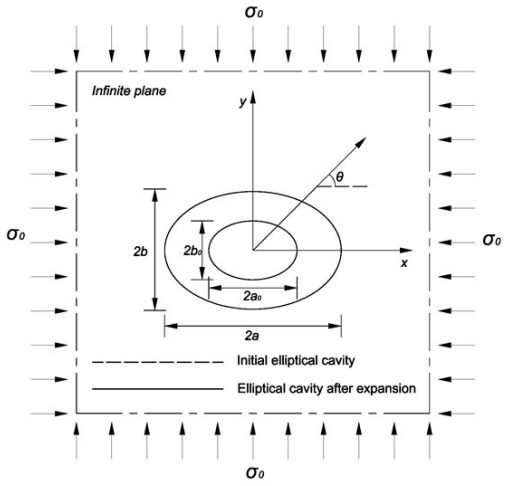

Figure 8. Schematic diagram of elliptical cavity expansion

$$z = \omega(\zeta) = R\left(\frac{1}{\zeta} + m\zeta\right) \tag{1}$$

where *R* and *m* are real numbers, depending on the elliptic semi-majar axis *a* and semi-minor axis *b*.

$$R = \frac{a+b}{2}, \quad m = \frac{a-b}{a+b} \tag{2}$$

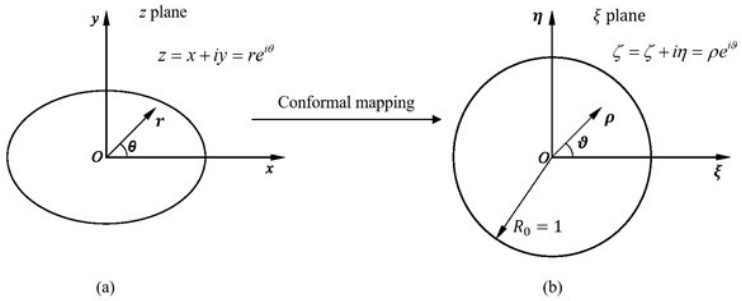

Figure 9. Schematic diagraph of conformal mapping**.**

In order to keep the shape ratio of elliptical cavity in expansion unchanged, the displacement at different positions should be a function of θ, as shown in Eq. (3)

$$u(\theta) = \frac{u_a}{\sqrt{1+\left(\beta_0^2 - 1\right)\sin^2\theta}} \tag{3}$$

where, u_a is the displacement along the direction of major axis and $\beta_0 = a/b$.

The displacement boundary condition in the physical plane need to be converted to the phase plane. The variable θ in the physical plane is different from the variable ϑ in the phase plane. The conversion between the two parameters is as follows:

$$\cos\theta = \frac{\left(\rho + m/\rho\right)\cos\vartheta}{\sqrt{\left(\rho + m/\rho\right)^2\cos^2\vartheta + \left(\rho - m/\rho\right)^2\sin^2\vartheta}} \qquad \sin\theta = \frac{\left(\rho - m/\rho\right)\sin\vartheta}{\sqrt{\left(\rho + m/\rho\right)^2\cos^2\vartheta + \left(\rho - m/\rho\right)^2\sin^2\vartheta}} \tag{4}$$

At the cavity boundary ($\rho = 1$),$m = \frac{\beta_0 - 1}{\beta_0 + 1}$. Eq. (4) can be rearranged as

$$\cos\theta = \frac{\cos\vartheta}{\sqrt{1 + \left(1/\beta_0^2 - 1\right)\sin^2\vartheta}} \qquad \sin\theta = \frac{\sin\vartheta}{\sqrt{1 + \left(\beta_0^2 - 1\right)\cos^2\vartheta}} \tag{5}$$

Therefore, the displacement boundary condition can be written as (in ζ plane)

$$g\left(\vartheta\right) = \frac{u_a}{\sqrt{\beta_0^2/\left[1 + \left(\beta_0^2 - 1\right)\cos^2\vartheta\right]}} \tag{6}$$

Conveniently, the Fourier transform of Eq. (6) were written as

$$F_0 = g\left(\vartheta\right) = \sum_{-\infty}^{\infty} f_k e^{ik\vartheta} = \sum_{-\infty}^{\infty} f_k \zeta^k \qquad f_k = \frac{1}{2\pi}\int_0^{2\pi} g\left(\vartheta\right) e^{-ik\vartheta}\mathrm{d}\vartheta \tag{7}$$

where F_0 is the Fourier series expansion expression of the displacement boundary condition, and f_k is the Fourier series coefficient.

3.1.3 Solving the stress function

Next, the stress function satisfying the boundary displacement condition needs to be solved. As no body force is applied, the plane strain problem of elasticity is attributed to solving the biharmonic equation of Airy stress function *U*.

$$\nabla^4 U = 0 \tag{8}$$

By introducing complex variable $z = x + iy$ and conjugate complex variable $\bar{z} = x - iy$ and substituting Eq. (8), the complex function representation of stress component can be obtained:

$$\begin{aligned} &\sigma_\theta + \sigma_r = 2\left[\Phi\left(\zeta\right) + \overline{\Phi\left(\zeta\right)}\right] = 4\,\mathrm{Re}\,\Phi\left(\zeta\right) \\ &\sigma_\theta - \sigma_r + 2i\sigma_{r\theta} = \frac{2\zeta^2}{\rho^2\overline{\omega'\left(\zeta\right)}}\left[\overline{\omega\left(\zeta\right)}\Phi'\left(\zeta\right) + \omega'\left(\zeta\right)\Psi\left(\zeta\right)\right] \end{aligned} \tag{9}$$

where, σ_ρ、σ_ϑ and $\sigma_{\rho\vartheta}$ are the radial stress, hoop stress and shear stress of any point in the ζ plane, respectively; Re is a real part of complex numbers, $\Phi\left(\zeta\right)$ and $\psi\left(\zeta\right)$ are complex potential functions, which can be obtained by Eq. (10)

$$\Phi\left(\zeta\right) = \varphi'\left(\zeta\right)/\omega'\left(\zeta\right) \qquad \Psi\left(\zeta\right) = \psi'\left(\zeta\right)/\omega'\left(\zeta\right) \tag{10}$$

where, $\varphi\left(\zeta\right)$ and $\psi\left(\zeta\right)$ are stress functions that can be solved by the displacement boundary condition.

According to Ref. [23], we have

$$2G\left(u+iv\right)=g\left(\vartheta\right)=\left(3-4\upsilon\right)\varphi\left(\zeta\right)-\frac{\omega\left(\zeta\right)}{\overline{\omega'\left(\zeta\right)}}\overline{\varphi'\left(\zeta\right)}-\overline{\psi\left(\zeta\right)}\Big|_{\zeta=\sigma} \tag{11}$$

where, G is shear modulus of the material, u and v are displacements in the direction ζ and η, respectively; υ is Poisson's ratio and $\sigma=e^{i\vartheta}$.

The stress functions $\varphi\left(\zeta\right)$ and $\psi\left(\zeta\right)$ are analytic and can be expressed as

$$\begin{aligned}\varphi\left(\zeta\right)&=\frac{1}{8\pi\left(1-\upsilon\right)}\left(F_x+iF_y\right)\ln\zeta+B\omega\left(\zeta\right)+\varphi_0\left(\zeta\right)\\ \psi\left(\zeta\right)&=\frac{3-4\nu}{8\pi\left(1-\upsilon\right)}\left(F_x-iF_y\right)\ln\zeta+\left(B'+iC'\right)\omega\left(\zeta\right)+\psi_0\left(\zeta\right)\end{aligned} \tag{12}$$

The vectors F_x+iF_y and F_x-iF_y represent the pressure applied to the initial cavity wall. In this paper, the two vectors are equal to zero. B and $B+iC'$ are related to the stress at infinity, and their values in this paper are zero [23]. Additionally, the functions $\varphi_0\left(\zeta\right)$ and $\psi_0\left(\zeta\right)$ are analytical at infinity and can be written as Laurent series. From Eq. (12), we obtain

$$\varphi\left(\zeta\right)=\varphi_0\left(\zeta\right)=\sum_{k=1}^{\infty}a_k\zeta^k\qquad\psi\left(\zeta\right)=\psi_0\left(\zeta\right)=\sum_{k=0}^{\infty}b_k\zeta^k \tag{13}$$

Substituting Eq. (7) into Eq. (11), we have

$$\left(3-4\upsilon\right)\varphi_0\left(\sigma\right)-\frac{\omega\left(\sigma\right)}{\overline{\omega'\left(\sigma\right)}}\overline{\varphi_0'\left(\sigma\right)}-\overline{\psi_0\left(\sigma\right)}=g\left(\vartheta\right)=2G\sum_{-\infty}^{\infty}f_k\sigma^k \tag{14}$$

Multiplying the term of $(1/2\pi i)(1/\sigma-\xi)$ at both sides of Eq. (14) and taking integration of Eq. (14) along the initial cavity wall, we can get

$$\frac{1}{2\pi i}\int\frac{\left(3-4\upsilon\right)\varphi_0\left(\sigma\right)}{\sigma-\zeta}d\sigma-\frac{1}{2\pi i}\int\frac{\omega\left(\sigma\right)}{\overline{\omega'\left(\sigma\right)}}\overline{\varphi_0'\left(\sigma\right)}\frac{1}{\sigma-\zeta}d\sigma-\frac{1}{2\pi i}\int\frac{\overline{\psi_0\left(\sigma\right)}}{\sigma-\zeta}d\sigma=\frac{1}{2\pi i}\int\frac{F_0}{\sigma-\zeta}d\sigma \tag{15}$$

By means of the Cauchy integral formula [23], the integral terms of Eq. (15) can be written as follows

$$\begin{aligned}&\frac{1}{2\pi i}\int\frac{\left(3-4\upsilon\right)\varphi_0\left(\sigma\right)}{\sigma-\zeta}d\sigma=\left(3-4\upsilon\right)\varphi_0\left(\zeta\right)\\ &\frac{1}{2\pi i}\int\frac{\omega\left(\sigma\right)}{\overline{\omega'\left(\sigma\right)}}\overline{\varphi_0'\left(\sigma\right)}\frac{1}{\sigma-\zeta}d\sigma=\frac{1}{2\pi i}\int\frac{\sigma^{-1}+m\sigma}{-\sigma^2+m}\sum_{k=1}^{\infty}k\overline{a_k}\sigma^{1-k}\frac{1}{\sigma-\zeta}d\sigma=0\\ &\frac{1}{2\pi i}\int\frac{\overline{\psi_0\left(\sigma\right)}}{\sigma-\zeta}d\sigma=0\quad and\quad\frac{1}{2\pi i}\int\frac{F_0}{\sigma-\zeta}d\sigma=2\mathrm{G}\sum_{k=0}^{\infty}f_k\zeta^k\end{aligned} \tag{16}$$

Substituting the Eq. (16) into Eq. (13) results in

$$\varphi_0\left(\zeta\right)=\frac{2\mathrm{G}}{\left(3-4\upsilon\right)}\sum_{k=0}^{\infty}f_k\zeta^k \tag{17}$$

Similarly, another stress function $\psi_0(\zeta)$ can also be obtained from Eq. (14)

$$\psi_0(\zeta)=(3-4\upsilon)\overline{a_0}-\frac{2\mathrm{G}}{(3-4\upsilon)}\frac{\zeta+m\zeta^{-1}}{-\zeta^{-2}+m}\sum_{k=1}^{\infty}kf_k\zeta^{k-1}-2\mathrm{G}\sum_{k=0}^{\infty}\overline{f_{-k}}\zeta^{k} \tag{18}$$

Substituting Eqs. (17) and (18) into Eq. (9), we get

$$\sigma_\vartheta+\sigma_\rho=4\,\mathrm{Re}\left(\frac{2G}{(3-4\upsilon)R}\frac{\sum_{k=1}^{\infty}kf_k\zeta^{k+1}}{(m\zeta^2-1)}\right) \tag{19}$$

$$\begin{aligned}\sigma_\vartheta-\sigma_\rho+2i\sigma_{\rho\vartheta}=\frac{2e^{2i\vartheta}}{R}\frac{1}{(m-\zeta^2)}\Bigg[&\frac{2G}{(3-4\upsilon)}\frac{(\zeta+m\zeta^{-1})\left[(m\zeta^2-1)\sum_{k=1}^{\infty}k(k+1)f_k\zeta^k-2m\zeta\sum_{k=1}^{\infty}kf_k\zeta^{k+1}\right]}{(m\zeta^2-1)^2}+\ldots\\&\frac{2G}{3-4\upsilon}\left(\frac{2(\zeta+m^2\zeta)}{(m\zeta^2-1)^2}\sum_{k=1}^{\infty}kf_k\zeta^k-\frac{(\zeta^2+m)}{(m\zeta^2-1)}\sum_{k=1}^{\infty}k^2f_k\zeta^{k-1}\right)-2G\sum_{k=1}^{\infty}k\overline{f_{-k}}\zeta^{k-1}\Bigg]\end{aligned} \tag{20}$$

The elastic field stress of material can now be solved by Eqs. (19) and (20).

3.1.4 Solving the cavity boundary stress olving the stress function

The region outside the elliptical cavity satisfies the plastic yield criterion. Under the plane strain assumption, the equilibrium equation without body force is

$$\begin{cases}\dfrac{\partial\sigma_\rho}{\partial\rho}+\dfrac{1}{\rho}\dfrac{\partial\sigma_{\rho\vartheta}}{\partial\vartheta}+\dfrac{\sigma_\rho-\sigma_\vartheta}{\rho}=0\\[2ex]\dfrac{\partial\sigma_{\rho\vartheta}}{\partial\rho}+\dfrac{1}{\rho}\dfrac{\partial\sigma_\vartheta}{\partial\vartheta}+\dfrac{2\sigma_{\rho\vartheta}}{\rho}=0\end{cases} \tag{21}$$

Assuming that the Von-Mises yield criterion is satisfied in the plastic zone, the ela-plastic boundary *c* can be obtained by substituting Eqs. (19) and (20) into Eq. (22).

$$\begin{cases}\dfrac{3}{2}(\sigma_\rho-\sigma_\vartheta)^2+6\sigma_{\rho\vartheta}^2<2Y^2 & \text{elastic}\\[2ex]\dfrac{3}{2}(\sigma_\rho-\sigma_\vartheta)^2+6\sigma_{\rho\vartheta}^2=2Y^2 & \text{elastic-plastic boundary}\\[2ex]\dfrac{3}{2}(\sigma_\rho-\sigma_\vartheta)^2+6\sigma_{\rho\vartheta}^2>2Y^2 & \text{plastic}\end{cases} \tag{22}$$

Integrating equation (21) in the plastic zone can obtain the plastic field stress distribution. As shown in Fig. 10, e_ρ and e_ϑ are base vectors in cylindrical coordinates and we have e_α and e_β base vectors which are normal and tangent to the surface, respectively. The actual direction of the stress is along the outer normal direction of the contour, and Eq. (21) needs to be transformed. Assuming that *l* is the distance along the direction of e_ϑ, then $dl=\rho d\vartheta$. therefore:

$$\begin{aligned}\frac{\partial}{\partial l}&=\frac{1}{\rho}\frac{\partial}{\partial \vartheta}\\ \frac{\partial}{\partial \beta}&=\frac{1}{\partial \rho}\cos\left(\rho,\beta\right)+\frac{\partial}{\partial l}\cos\left(l,\beta\right)\end{aligned} \tag{23}$$

where, $\cos\left(\rho,\beta\right)$ and $\cos\left(l,\beta\right)$ are directional cosines.

Eq. (21) can be rearranged as

$$\begin{aligned}&\frac{\partial}{\partial \rho}\left(\sigma_{\rho}-\frac{\sin\gamma}{\cos\gamma}\sigma_{\rho\vartheta}\right)+\frac{1}{\cos\gamma}\frac{\partial \sigma_{\rho\vartheta}}{\partial \beta}+\frac{\sigma_{\rho}-\sigma_{\vartheta}}{r}=0\\ &\frac{\partial}{\partial \rho}\left(\sigma_{\rho\vartheta}-\frac{\sin\gamma}{\cos\gamma}\sigma_{\vartheta}\right)+\frac{1}{\cos\gamma}\frac{\partial \sigma_{\vartheta}}{\partial \beta}+\frac{2}{\rho}\sigma_{\rho\vartheta}=0\end{aligned} \tag{27}$$

where, the angle γ depends on the geometry of the contour.

On both sides of the elastic-plastic boundary, stress and displacement are continuous. As shown in Fig. 11, assuming that the elastic-plastic boundary contour is Γ_{s+1}, the stress and displacement of the next node on the plastic zone contour Γ_s can be obtained by iterative equilibrium equation. $(\sigma_\rho)_{j^s}$、 $(\sigma_\vartheta)_{j^s}$ and $(\sigma_{\rho\vartheta})_{j^s}$ can be obtained by

$$\begin{aligned}&\frac{1}{\Delta\rho}\left[\left\{\left(\sigma_{\rho}\right)_{j^{s+1}}-\left(\sigma_{\rho}\right)_{j^{s}}\right\}-\tan\gamma\left\{\left(\sigma_{\rho\vartheta}\right)_{j^{s+1}}-\left(\sigma_{\rho\vartheta}\right)_{j^{s}}\right\}\right]\\ &\qquad+\frac{1}{\cos\gamma}\frac{\left(\sigma_{\rho\vartheta}\right)_{j^{s+1}+1}-\left(\sigma_{\rho\vartheta}\right)_{j^{s+1}+1}}{\Delta\beta}+\frac{\left(\sigma_{\rho}\right)_{j^{s+1}}-\left(\sigma_{\vartheta}\right)_{j^{s+1}}}{\rho_{j^{s+1}}}=0\end{aligned} \tag{25}$$

$$\begin{aligned}&\frac{1}{\Delta\rho}\left[\left\{\left(\sigma_{\rho\vartheta}\right)_{j^{s+1}}-\left(\sigma_{\rho\vartheta}\right)_{j^{s}}\right\}-\tan\gamma\left\{\left(\sigma_{\rho\vartheta}\right)_{j^{s+1}}-\left(\sigma_{\rho\vartheta}\right)_{j^{s}}\right\}\right]\\ &\qquad+\frac{1}{\cos\gamma}\frac{\left(\sigma_{\vartheta}\right)_{j^{s+1}+1}-\left(\sigma_{\vartheta}\right)_{j^{s+1}+1}}{\Delta\beta}+\frac{2}{\rho_{j^{s+1}}}\left(\sigma_{\rho\vartheta}\right)_{j^{s+1}}=0\end{aligned} \tag{26}$$

where, $\frac{1}{\Delta\beta}=\frac{1}{\Delta\rho}\sin\gamma+\frac{1}{\rho\Delta\vartheta}\cos\gamma$.

The plastic field stress of material can now be solved by Eqs. (25) and (26).

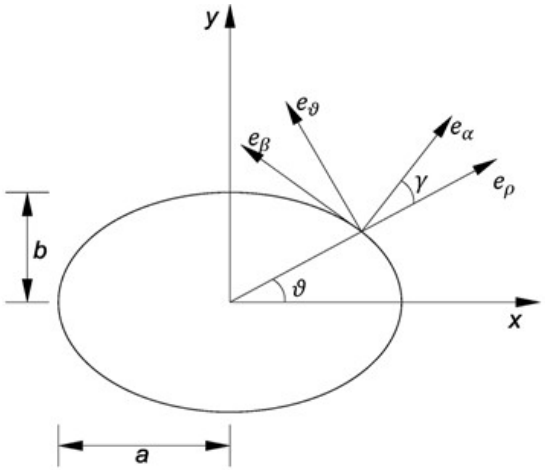

Figure 10. Schematic diagram of orthogonal and polar coordinate system.

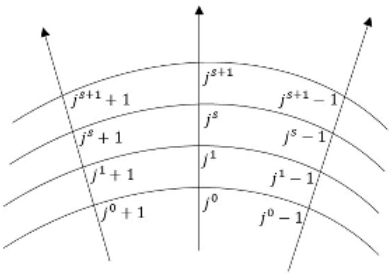

Figure 11. Schematic diagram of orthogonal and polar coordinate system.

3.2 Validation of elliptical cavity expansion model

3.2.1 The displacement boundary condition expressed by the stress function

In the above solving process, the displacement boundary condition is expressed in three forms: the displacement boundary condition derived from assumption 3 (Eq. (6)), the Fourier series expansion of the displacement boundary condition (Eq. (7)) and the displacement boundary condition expressed by the stress function (Eq. (11)). Therefore, when the Fourier series expansion of the displacement boundary condition and the stress function solved by Eqs. (17) and (18) are correct, Eq. (6)、Eq. (7) and Eq. (11) are three expressions of the same function, and the curves drawn according to three formulas should be consistent. When $u_a = 1cm$,*G*=7.86GPa, $\upsilon = 0.5$, $Y = 40\text{MPa}$ and $\beta = 2$, the curves are shown in Fig. 12. It can be seen from the figure that the three curves basically coincide, which proves the correctness of the stress function.

3.2.2 Comparison between model degenerate solution and Kirsch problem results

When *a* and *b* in Eq. (1) are equal, the model can map the outside of the circle with radius R to the outside of the unit circle. Using the conformal transformation formula, the above derived formula can be used to obtain the degenerate solution of elliptical cavity expansion-circular cavity expansion. Muskhelishvili [23] gives the analytical solution of the elastic field stress of the material when the circular cavity expands to a certain distance *u* (Kirsch problem), so the reliability of the solution in this paper is verified by the degenerate solution. The stress components calculated by the method in this paper are

$$\sigma_\rho = -\sigma_\vartheta = \frac{2GuR}{\rho^2}, \quad \sigma_{\rho\vartheta} = 0 \tag{27}$$

$$u_r = uR/\rho \tag{28}$$

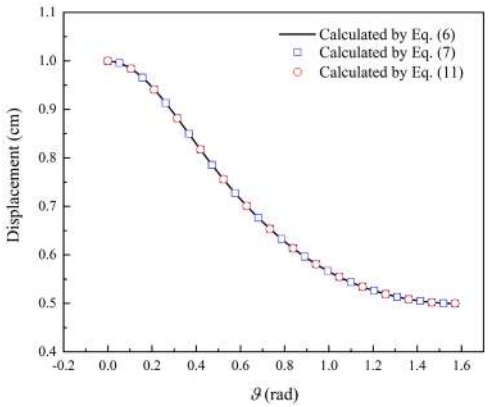

Figure 12. Verification of the displacement boundary condition.

Fig. 13 shows the radial stress σ_ρ, hoop stress σ_ϑ and radial displacement u_r along the radial distribution of the calculation results in this paper compared with the calculation results of Muskhelishvili, this is completely consistent with the theoretical solution of Muskhelishvili.

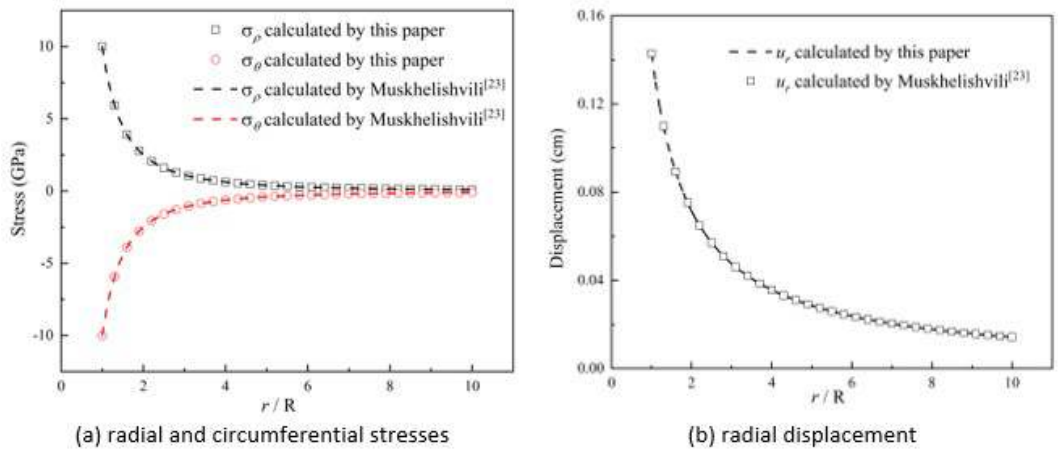

Figure 13. Comparison between the calculation results and Kirsch problem results [23].

3.3 Penetration depth analysis of the ECSP penetrating concrete target

3.3.1 Radial stress distribution characteristics of elliptical cavity boundary

Fig. 14 shows the calculation results of radial stress on the elliptical cavity boundary when the parameters are consistent with section 3.2.1. The radial stress is divided by the yield strength of the material so that the effect of the yield strength of the material on the calculation results can be eliminated, as shown in Fig. 14a.

Dong et al. [18] studied the radial stress distribution of ECSP with different striking velocities penetrating concrete target by numerical simulation. The results show that the radial stress at the projectile nose increases progressively from the minor axis to the major axis. In addition, in the process of projectile penetration, the nose of projectile always maintains the process of expanding from small elliptical cavity to large elliptical cavity with equal shape ratio. The displacement required in the major axis of the elliptical cavity is larger than that in the minor axis. Therefore, it is reasonable that the stress in the major axis of the elliptical cavity is larger than that in the minor axis. The calculation results of the semi-analytical model in this paper also have the same law.

Defined the stress distribution coefficient *k* (Fig. 14b) as the stress distribution of equal proportion expansion of the cavity of elliptic cross-section divided by the stress value required for the cavity of circular cross-section to expand the same distance and assuming that the stress distribution coefficient *k* of the projectile nose remains unchanged during the whole tunnel phase of penetration. Namely, *k* is related to the cross-section shape of the projectile and material properties of the target, but not to the striking velocity.

Specifically, with the parameters in section 3.2.1, the means of the stress distribution coefficient *k* is $3.84\sigma_\rho/Y$ and the stress value required for the cavity of circular cross-section to expand the same distance is $3.66\sigma_\rho/Y$. This means that due to the asymmetric stress distribution on the elliptical cavity boundary, the penetration resistance of the ECSP is larger than that of the CCSP with the same cross-section area

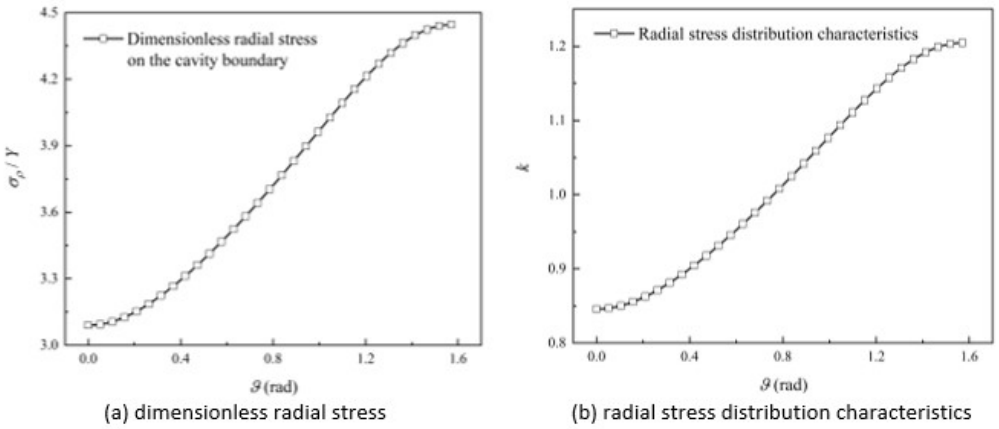

Figure 14. Radial stress distribution characteristics of elliptical cavity boundary.

3.3.2 Prediction model of penetration-depth

When the projectile velocity is lower than the critical velocity, in order to simplify the analysis process, the theoretical model generally assumes that the projectile is rigid body. After exceeding the critical velocity, the penetration is dominated by a semi-hydrodynamic regime. From the relevant research results [29,30] and the recovered projectile in this paper, it can be concluded that the projectile velocity does not exceed the critical velocity, and is still in the stage of rigid penetration.It is well known that the process of projectile penetrating into concrete target can be divided into two stages. Forrestal et al. [31] proposed that the depth of the crater area can be expressed by 2D when the projectile penetrates the concrete medium. The penetration resistance in the first stage is

$$F_z = Cz_0, \quad 0 \le z_0 \le 2D \tag{29}$$

where *C* is the parameter in Ref. [31], *D* is diameter of the projectile and z_0 is the axial position, as shown in Fig. 15.

At the second stage, the resistance of the projectile can be obtained by integrating σ_n over the projectile nose. χ is the angle between the z_0 axis and the normal direction of the microelement of projectile nose d*s*. It should be noted that for the CCSP, the value of χ is constant in the circumferential direction for a fixed penetration position z_0, but for the ECSP, the value of χ is related to α. The axial resistance of the projectile F_z is determined by combining the normal stress and friction force acting on the nose of the projectile. As mentioned earlier, the surface stress of the nose σ_n can be expressed by the traditional sphere cavity expansion model (SCE) [31] combined with the stress distribution coefficient *k*.

$$\frac{\sigma_n}{Y} = k \cdot \left[a_1 \cdot \left(\frac{v_n}{\sqrt{Y/\rho_c}} \right)^2 + a_2 \cdot \frac{v_n}{\sqrt{Y/\rho_c}} + a_3 \right] \tag{30}$$

where, a_1, a_2 and a_3 are inertial, viscosity and strength coefficients, respectively [31, 32]. ρ_c is the density of concrete targets and v_n is the normal velocity of the projectile.

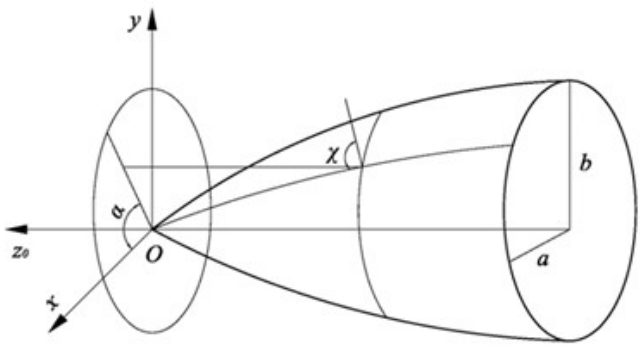

Figure 15. The resistance calculation model of the ECSP [18].

The normal velocity v_n and striking velocity v_0 of the projectile have the following relationship: $v_n = v_0 cos\chi$. In the meantime, there is friction in the process of projectile penetration, the relationship between shear stress σ_t and friction coefficient μ is: $\sigma_t = \mu\sigma_n$.

The axial resistance F_z can finally be expressed as

$$F_z = \int_S \sigma_n \left(\cos\chi + \mu \sin\chi \right) \mathrm{d}S \tag{31}$$

where *S* is the nose surface area of the projectile, μ is 0.01 [33], and F_z can be obtained by integration

$$F_z = A_1 v_0^2 + A_2 v_0 + A_3 \tag{32}$$

where, A_1, A_2 and A_3 are integration constant.

The kinematic equation for the projectile with a mass m_0 is

$$m_0 \frac{d^2 z_0}{dt^2} = -F_z = -\begin{cases} Cz_0 & 0 \le z_0 \le 2D \\ A_1 v^2 + A_2 v + A_3 & z_0 > 2D \end{cases} \tag{33}$$

Finally, the penetration depth *P* of the ECSP penetrating concrete target can be calculated by integral Eq. (33).

4 Penetration-depth predictions for circular and elliptical cross-section projectiles

In this section, the accuracy of penetration-depth prediction model in section 3 is verified by the experiment data in section 2 and Refs. [17, 18]. Table 3 shows the comparison between predictions and the experimental data, and ε represents the deviation of predictions from the experiment data. The predictions agree well with the experiment data, and the maximum deviation is 14.28%.

Fig. 16 shows the comparison between the predicted penetration depth in this paper and the experiment data with striking velocities ranged from 500 m/s to 1100 m/s. It can be seen from the prediction results that CCSPs (C1) have almost the same mass as ECSPs (E2-1), but in the striking velocity range of 500 m/s to 1100 m/s, the C1 projectile has a slight advantage in penetration depth, and the penetration depth of the CCSP is 6%~8% more than that of the ECSP at the same striking velocity, and with the increase of striking velocity, the difference of penetration depth between two types of projectiles increases progressively.

Table 3. Comparison of the penetration depth.

Test NO.	Type	Striking velocity (m/s)	Mass (g)	Depth (m)		ε(%)
				Experiment	Prediction	
1	C1	740	455	0.529	0.563	6.43
2	C1	767	453	0.599	0.596	-0.05
3	C1	593	452	0.347	0.379	9.22
4	C1	577	453	0.351	0.361	0.28
5	E1	609	432	0.311	0.303	-2.57
6	E1	/	/	/	/	/
7	E1	741	431	0.422	0.423	0.02
8	E1	750	431	0.472	0.441	-6.57
9	E2-1	764	449	0.517	0.548	5.99
10	E2-1	760	449	0.534	0.543	1.68
11	E2-1	605	452	0.427	0.366	-14.28
12	E2-1	578	453	0.362	0.339	-6.35
13	E2-2	850	341	0.504	0.477	-5.36
14	E2-2	1036	341	0.670	0.668	-0.03
15	E2-2	716	339	0.360	0.353	-1.94
16	E2-2	955	339	0.586	0.578	-1.37

To verify the accuracy of the model, experimental data [17, 18] are used to compare with the theoretical model and the results are shown in Table 4 and Fig. 17. Although there are differences in the projectile parameters and striking velocities, the penetration-depth predictions agree well with the experiment data and the maximum deviation is 14.56% and the calculation results show that the present model in this paper has good generalization.

Table 4. Comparison of the penetration depth of existing experiment data.

Test NO.	Type	Velocity (m/s)	Mass (g)	Depth (m)		ε(%)
				Experiment	Prediction	
1	E3	755	448.0	0.573	0.538	-6.10
2	E3	747	450.0	0.553	0.531	-3.98
3	E3	748	447.0	0.570	0.529	-7.19
4	E4	714	451.0	0.462	0.418	-9.52
5	E4	740	453.0	0.472	0.442	-6.36
6	E4	740	452.0	0.471	0.441	-6.37
7	E5	748	222.4	0.408	0.390	-4.41
8	E5	879	222.8	0.530	0.520	-1.89
9	E5	943	222.6	0.588	0.589	0.02
10	E5	1045	222.6	0.728	0.706	-3.02
11	E5	1057	222.4	0.725	0.719	-0.08
12	E6	728	222.8	0.380	0.343	-9.74
13	E6	835	222.5	0.491	0.436	-11.20
14	E6	934	222.7	0.596	0.530	-11.07
15	E6	1069	222.1	0.783	0.669	14.56

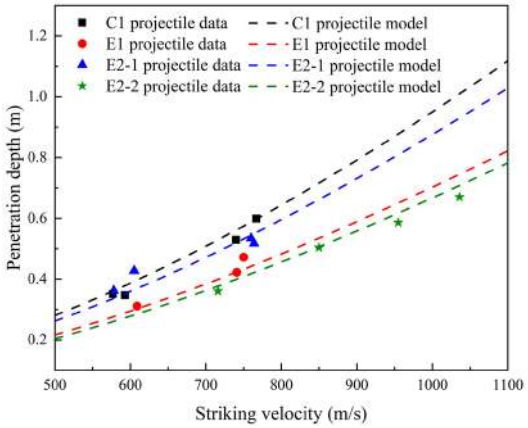

Figure 16. Experiment and predictions data.

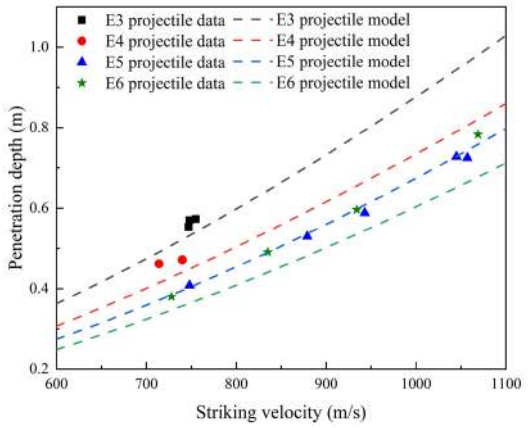

Figure 17. Existing experiment and predictions data.

5 Analysis and discussions

The shape ratio β_0 and CRH of projectile are the main factors that influence the penetration performance at the given projectile mass and target material. In this section, the influence of shape ratio β_0 and CRH of projectile on penetration performance are analyzed by taking some projectiles with different structures as computational model

based on the validation in section 4. In addition, the ECSP is suitable for hypersonic weapon platform. Base on HIFiRE-4 boost-gliding hypersonic platform, the application prospect of the ECSP is studied.

5.1 Influence of shape ratio on penetration performance

The correctness of the theoretical model has been verified by abundant experimental data. The most representative feature of the ECSP is its shape ratio. In order to study the influence of shape ratio on the penetration performance of ECSP, five types of projectile with shape ratios from 1 to 2 are designed. When the shape ratio is 1, the projectile becomes an ordinary CCSP. Except for shape ratio, the mass, length and cross-section area of the five projectiles are consistent. Fig. 18 shows the penetration depth of five projectiles with striking velocities ranged from 500 m/s to 1200 m/s. At the same striking velocity, the projectile with larger shape ratio has lower penetration depth. In this striking velocity range, the penetration depth of the ECSP with shape ratio of 2 is about 15% lower than that of the CCSP.

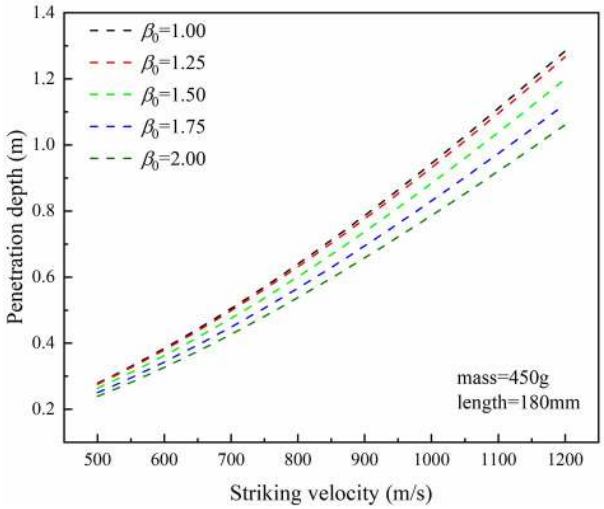

Figure 18. Penetration depth vs Striking velocity with different shape ratios.

The ECSP exhibits lower penetration performance than the CCSP. In order to analyze the reasons for the difference, the radial stress distribution of two typical cross-sections of the five projectiles are extracted, and the cross-section positions are 1/3 and 2/3 of the projectile nose length from the projectile tip, respectively. The striking velocity is set at 800 m/s and the remaining parameters are consistent with section 3. The dimensionless radial stress is shown in Fig. 19, it can be found the radial stress distribution of ECSP is significantly different from that of CCSP, showing a gradual increase from the minor axis direction to the major axis direction, which is similar to the sinusoidal distribution. However, the radial stress distribution is not completely symmetrical. The area surrounded by the curve in Fig. 19 represents the resistance of the section. If the radial stress distribution is completely symmetrical, the penetration performance of the ECSP and the CCSP should be equivalent, because their integral areas are equal.

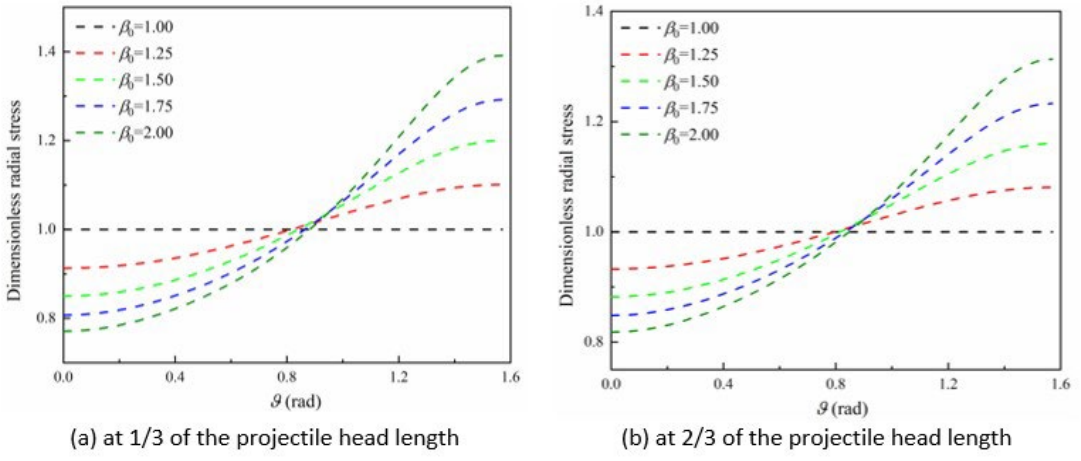

Figure 19. The dimensionless radial stress distribution of projectiles with different shape ratios.A

The ratios of penetration resistance F_z of five projectiles to penetration resistance of CCSP are 1, 1.018, 1.06, 1.12 and 1.19. It can be seen that the penetration resistance of ECSPs is higher than that of CCSPs, and the increase amplitude of penetration resistance increases with the increase of shape ratio. Therefore, under the same conditions, the CCSP has the optimal penetration performance.

5.2 Influence of the CRH on penetration performance

The penetration performance of the CCSP significantly depends on the CRH. As discussed in Refs. [34, 35], a CCSP with a larger CRH has better penetration performance. In order to study the penetration performance of ECSPs with different CRH, six typical projectiles are designed, and their structural parameters are shown in Table 5. C1, S1 and Z1 represent oval-nosed projectile, sphere-shaped projectile and cone-shaped projectile, respectively. The suffix E represents that the cross-section shape of the projectile is an ellipse with a shape ratio of 2.

Table 5. Main parameters of six typical projectiles.

Name	Part contour of the projectile	2a(D) (mm)	2b(D) (mm)	Shape ratio	CRH	Mass (g)	Length (mm)
C1		24	24	1	6.11	450	144
C1-E		33.94	16.97	2	11.97	450	144
S1		24	24	1	0.5	450	144
S1-E		33.94	16.97	2	0.75	450	144
Z1		24	24	1	\	450	144
Z1-E		33.94	16.97	2	\	450	144

The penetration depths of six projectiles calculated by the theoretical model are shown in Fig. 20. For the oval-nosed projectile, the law is consistent with Section 5.1, and the penetration depth of the ECSP (E1-E) is lower than that of the corresponding CCSP (C1). Similarly, the cone-shaped projectile (Z1) is similar to the oval-nosed projectile, and the penetration performance decreases when the cross-section shape of the projectile becomes ellipse (Z1-E), which indicates that the elliptical cross-section affects the force distribution of the projectile, resulting in an increase in the penetration resistance.

However, sphere-shaped projectile (S1) appear to show different laws from oval-nosed projectile and cone-shaped projectile. When the cross-section shape of the projectile becomes ellipse (S1-E), the penetration performance has a slight improvement. It is noted that when the cross-section shape of the projectile becomes ellipse, the value of CRH of oval-nosed projectile and sphere-shaped projectile increases. According to Ref. [32], the increase of CRH will strengthen the penetration performance of the projectile, which may be the reason why the penetration performance of S1-E projectile is slightly better than that of S1 projectile.

Therefore, two projectiles (C2-E and S2-E) are added to compare and analyze the influence of CRH and shape ratio β_0 on penetration performance. C2-E projectile is similar to C1-E projectile, and the shape ratio is 2. By reducing the length of the projectile head, the value of CRH of C2-E projectile is consistent with C1 projectile, and the design method of S2-E projectile is the same. The penetration depths of the six projectiles are shown in Fig. 21. The penetration performance of C2-E projectile and S2-E projectile is the lowest, and their CRH are consistent with that of C1 projectile and S1 projectile, which indicates that after the projectile cross-section shape becomes ellipse, the penetration resistance increases due to the asymmetry of stress distribution. The penetration performance of C1-E and S1-E projectiles is better than that of C2-E and S2-E projectiles because of the influence of CRH. This also explains the reason why the penetration

performance of S1-E projectile is slightly better than that of S1 projectile. The increase of CRH improves the penetration performance, and the increase of shape ratio β_0 reduces the penetration performance. The value of CRH and shape ratio collectively determine the penetration performance of projectile.

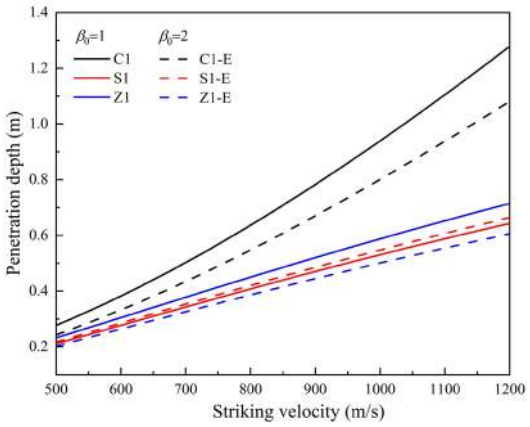

Figure 20. Penetration depth vs Six typical projectiles.

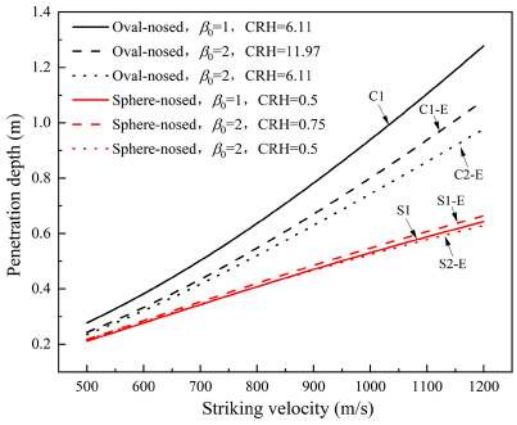

Figure 21. The influence of CRH and β_0 on penetration performance

5.3 Applicative prospect

Hypersonic weapon platform is usually a flat waverider structure to meet its aerodynamic performance. If the projectile installed on the weapon platform is an ECSP instead of a CCSP, the installation space can be used more effectively. The mass of the projectile can be increased by increasing its size, and the initial kinetic energy of penetrating the target can be finally increased. Based on the HIFiRE-4 hypersonic weapon platform, a CCSP and an ECSP are designed to meet the size of the platform, which are used to study the application prospect of the ECSP in the hypersonic weapon platform.

The cross-section size of the cabin of HIFiRE-4 hypersonic weapon platform is about 512×192 mm, as shown in Fig. 22. The minor axis of the two designed projectiles is tangent to the edge of the platform. The diameter of the CCSP (C3) is 192 mm, while the minor axis length of the ECSP (C3-E) is 192 mm, and the major axis length is 396 mm, and the shape ratio is 2.0625. Both the thickness of projectiles are 20 mm and filled with explosives. The calculation shows that the explosive area of the CCSP and the ECSP is 18145 mm^2 and 42499 mm^2, respectively, and the explosive area of the ECSP increases by 206%. From the perspective of charge area, due to the unique shape of ECSPs, it has an excellent application prospect in hypersonic weapon platform.

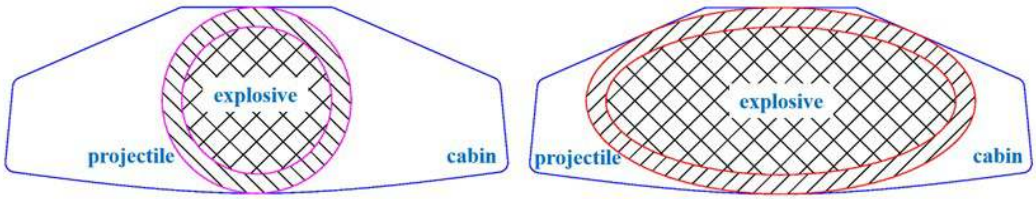

Figure 22. Cross-section diagram of HIFiRE-4 platform and designed projectiles.

According to the area ratio of the projectile and explosive, the mass ratio of the two projectiles is estimated to be 1.8, assuming that the total mass of the CCSP is 100 kg and the value of CRH is 6.11, so the mass of the ECSP is 180 kg. Notably, due to the strong power of the hypersonic weapon platform, the hypersonic weapon platform is able to load the projectile with larger mass. Therefore, the initial velocity of the ECSP can be equivalent to than the CCSP. The target parameters are consistent with section 4 and the penetration depth of two projectiles with different striking velocities as shown in Fig. 23. It can be seen from the figure that the ECSP (C3-E) makes up for the lack of penetration performance caused by structure through total mass m_0, and the penetration performance is better than that of the CCSP (C3), and the gap of penetration depth increases with the increase of striking velocity.

Although the above calculation has highly hypothetical, the calculation results still strongly prove that the ECSP is more suitable for hypersonic weapon platforms in terms of charge quantity and penetration performance.

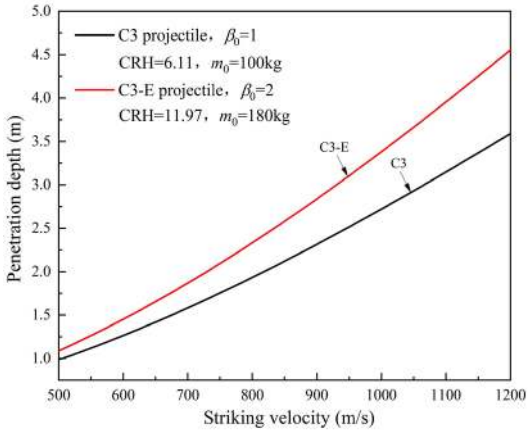

Figure 23. Comparison of penetration performance between C3 and C3-E projectiles.

6 Conclusions

The penetration characteristics of the ECSP into semi-infinite concrete target was studied. Experiments of CCSP and two types of ECSPs with shape ratios of 1.25 and 1.56 were conducted with striking velocities ranged from 550 m/s to 1050 m/s. A formula for predicting penetration depth was developed by combining with the force characteristics on the projectile nose and the semi-analytical model based on the theory of complex variable function and conformal transformation. The experimental and calculation results coincided fairly well. Further researches on the influences of shape ratio and CRH on penetration performance were conducted, and the application prospect of the ECSP on hypersonic weapon platform were studied as well.

(1) The experimental results showed that ECSPs exhibit excellent penetration behavior and trajectory stability with striking velocities ranged from 550 m/s to 1050 m/s.

(2) The semi-analytical model controlled by the displacement boundary condition can calculate the radial stress distribution characteristics of elliptical cross-section cavity and the calculation results show that the radial stress of elliptical cross-section cavity increases progressively from the minor axis to the major axis.

(3) The proposed model was validated by comparing the predicted penetration depths with 30 groups of experiment data, and the maximum deviation was 14.56%.

(4) With the increase of shape ratio and the decrease of the value of CRH, the penetration performance of the ECSP decreases gradually.

(5) Based on the HIFiRE-4 hypersonic weapon platform, compared with the CCSP, the mass and charge quantity of the ECSP are increased by 1.8 times and 2.06 times respectively, which has better penetration performance and damage effect.

In conclusion, the research results can be used in the design of non-circular cross-section projectile and solve the ballistic deflection problem of the ECSP penetrating the target. The penetration characteristics of ECSPs, especially the dynamic analytical solution of circumferential stress distribution on the head surface of projectiles and the ballistic trajectory deflection problem, remains to be further explored.

Acknowledgements

This work was supported by the Fundamental Research Funds for the Central Universities [No. 30919011401].

Author's Contribuitions: Writing - original draft, J Liu; Test technical support, X Zhang; Writing - review & editing, C Liu, H Wei.

Editor: Marcílio Alves.

References

[1] Vedernikov Y.A., Khudyakov Y.S., (2005). Evolution and comparative analysis of group armor and aeroballistics of ancient and modern ruled and poly-wedge arrows. Math Model Geoph 10:93–116.

[2] Bless S.J., (1996). Penetration mechanics of non-circular rods. American Institute of Physics 1996;370:1119-1122.

[3] Du Z.H., Zhu J.S., Wang X.Z., et al (2009). Analytical Model on Non-circular Penetrator Impacting Semi-infinite Target.Acta Armamentarii 4:403-407. (in chinese)

[4] Yankelevsky D.Z., Adin M.A., (1980). A simplified analytical method for soil penetration analysis. International journal for numerical and analytical methods in geomechanics 4(3):233-254.

[5] Feldgun V.R., Yankelevsky D.Z., Karinski Y.S., (2017). A new simplified analytical model for soil penetration analysis of rigid projectiles using the Riemann problem solution. International Journal of Impact Engineering 101:49-65.

[6] Luk V.K., Forrestal M.J., (1987). Penetration into semi-infinite reinforced-concrete targets with spherical and ogival nose projectiles. International Journal of Impact Engineering 6(4):291-301.

[7] Forrestal M.J., Luk V.K., (1992). Penetration into soil targets. International Journal of Impact Engineering 12(3):427-444.

[8] Bishop R.F., Hill R, Mott N.F., (1945). The theory of indentation and hardness experiments. Proceedings of the Physical Society 57(3):147-159.

[9] Ben-Dor G., Dubinsky A., (1997). Optimal 3D impactors penetrating into layered targets. Theor Appl Fract Mech 27(3):161–6.

[10] Ben-Dor G., Dubinsky A., (2002). A model for predicting penetration and perforation of FRP laminates by 3-D impactors. Composite Structures 56(3):243-248.

[11] Yakunina G.Y., (2020). The optimum non-conical and asymmetrical three-dimensional configurations. JOURNAL OF Mechanics and applied mathematics 64(4):583–91.

[12] Yakunina G.Y., (2000). The construction of optimum three-dimensional shapes within the framework of a model of local interaction. Journal of Applied Mathematics and Mechanics 64(2):289–98.

[13] Dhaliwal R.S., Singh B.M., (1978). The axisymmetric boussinesq problem of an initially stressed neo-hookean half-space for punch of arbitrary profile. International journal of engineering science 16(6):379-385.

[14] HYUNG. Cavity expansion analysis of non-circular cross-sectional penetration problems. Austin: The University of Texas; 1997. p. 56-85.

[15] Walter T.A., Wolde-Tinsae A.M., (1984). Turbine Missile Perforation of Reinforced Concrete. Journal of Structural Engineering 110(10):2439–55.

[16] Ben-Dor G., Dubinsky A., et al (2006). Applied high-speed plate penetration dynamics. Springer Netherlands 132(4):213-240.

[17] Wang W.J., Zhang X.F., Deng J.J., Zheng Y.M., Liu C., (2018). Analysis of projectile penetrating into mortar target with elliptical cross-section. Explosion and Shock Waves 38:164-73. (in chinese)

[18] Dong H., LIU Z.H., WU H.J., et al (2019). Study on penetration characteristics of high-speed elliptical cross-sectional projectiles into concrete. International Journal of Impact Engineering 132:1-12.

[19] Dong H., WU H.J., et al (2020). Penetration characteristics of pyramidal projectile into concrete target. International Journal of Impact Engineering 143:1-14.

[20] Liu Z.H., Wu H.J., Gao X.D., Pi A.G., Huang F.L., (2019). Study on the resistance characteristics of elliptical cross-section ogive-nose projectile penetrating concrete. Transaction of Beijing Institute of Technology 39:135-6. (in chinese)

[21] Dai X.H., Wang K.H., Li M.R., et al (2021). Rigid elliptical cross-section ogive-nose projectiles penetration into concrete targets. Defence Technology 7(3):1-12.

[22] Zhou H., Kong G.Q., Liu H.L., (2016). Pressure-controlled elliptical cavity expansion under anisotropic initial stress:Elastic solution and its application. Science China-Earth Sciences 7:1-20.

[23] Muskhelishvili NI., (1995). Some Basic Problems of the Mathematical Theory of Elasticity, american mathematical monthly.

[24] Chen X.W., Li Q.M., et al (2018). Penetration trajectory of concrete targets by ogived steel projectiles experiments and simulations. International Journal of Impact Engineering 120:202-213.

[25] Chen X.W., (2009). Advances in the penetration/ perforation of rigid projectiles. Advances in Mechanics 39(3):316-351.

[26] Galin L.A., (1946). Plane elasticplastic problem: plastic regions around circular holes in plates and beams. QUARTERLY JOURNAL OF MECHANICS AND APPLIED MATHEMATICS 10:777-783.

[27] Detournay E., (1986). An approximate statical solution of the elastoplastic interface for the problem of Galin with a cohesive-frictional material. International journal of solids and structures 22(12):1435-1454.

[28] Zhuang P.Z., YU H.S., (2019). Two-dimensional elastoplastic analysis of cylindrical cavity problems in Tresca materials. International journal for numerical and analytical methods in geomechanics 2:1-20.

[29] Liu C., Zhang X.F., Chen H.H., et al (2020). Experimental and theoretical study on steel long-rod projectile penetration into concrete targets with elevated impact velocities[J]. International Journal of Impact Engineering 138:103482.

[30] He X., Xu X.Y., Sun G.J., et al (2010). Experimental investigation on projectiles high-velocity penetration into concrete targets. Explosion Shock Waves 30(1): 1-6.

[31] Forrestal M.J., Frew D.J., et al (2003). Penetration of concrete targets with deceleration-time measurements. International Journal of Impact Engineering 28(5):479–97.

[32] Zhang S., et al (2017). High-velocity penetration of concrete targets with three types of projectiles: experiments and analysis. Latin American Journal of Solids and Structures 14(9):1614–28.

[33] Yinan W., (2009). The mechanism of high-speed kinetic energy projectile penetration into concrete. Transaction of Beijing Institute of Technology. (in chinese)

[34] Frew D.J., Forrestal M.J., Cargile J.D., (2006). The effect of concrete target diameter on projectile deceleration and penetration depth. International Journal of Impact Engineering 32:1584-94.

[35] Chen X.W., Li Q.M., (2002). Deep penetration of a rigid projectile with different geometrical characteristics. International Journal of Impact Engineering 27:619-37.